ISSN 2616-5880 Vol. 7, Issue 1: 26-33, DOI: 10.25236/AJMC.2026.070105

First-Principles Study of the Photocatalytic Echanism Based on the g-C_3N_4/Bi_2MoO_6 (010) Heterojunction

Huihui Shi[1,a], Shiheng Xin[1,b], Fuchun Zhang[1,c,*]

[1]*School of Physics and Electronic Information, Yan'an University, Yan'an, 716000, China*
[a]*shihui@yau.edu.cn,* [b]*shihengxin@yau.edu.cn,* [c]*yadxzfc@yau.edu.cn*
[*]*Corresponding author*

Abstract: *Density functional theory (DFT) is employed to study the electronic structures and properties of the g-C_3N_4/Bi_2MoO_6 (BMO) (010) heterojunction, and the energy band, density of states (DOS), and charge transfer properties are analyzed to reveal the microscopic mechanism. Band structure calculations reveal that the g-C_3N_4/Bi_2MoO_6(010) heterojunction possesses a direct band gap, which is substantially narrower than those of its individual g-C_3N_4 and BMO constituents, thereby facilitating electron transition and significantly enhancing its visible-light absorption. Analysis of the DOS reveals that the valence band maximum (VBM) of the heterojunction primarily originates from the N 2p orbitals of g-C_3N_4, while the conduction band minimum (CBM) is mainly composed of the Bi 6p and Mo 4d orbitals of Bi_2MoO_6. The different orbitals at VBM and CBM enable effective separation of electron-hole pairs, which significantly reduces the charge carrier recombination. Furthermore, analysis of the charge density difference and work function reveals a clear interfacial charge redistribution at the g-C_3N_4/Bi_2MoO_6(010) interface, which effectively promotes the separation of photogenerated carriers and inhibits their recombination. These findings provide a crucial theoretical foundation for guiding the design of high-performance photocatalytic heterostructures and highlight their significant potential for practical applications.*

Keywords: g-C_3N_4, Bi_2MoO_6, *Heterojunction, Density Functional Theory, Photocatalysis*

1. Introduction

The increasing prominence of environmental deterioration and global energy shortages has garnered widespread global attention[1]. This has led to the development of research hotspots in the field of photocatalysis centered on organic pollutant degradation and photocatalytic water splitting for H_2 evolution[2]. Consequently, the development of semiconductor photocatalysts with high solar energy conversion efficiency has become a research imperative[3-4]. Although semiconductor photocatalysis technology offers broad applicability in energy and environmental applications, its development is currently constrained by the intrinsic performance of photocatalysts. Because the bandgap is relatively large, photocatalysts can only respond to ultraviolet light, which accounts for a very low proportion of sunlight, and the utilization efficiency of the visible spectrum is relatively low. Furthermore, the rapid recombination and short lifetimes of photogenerated electron-hole pairs hinder their effective participation in catalytic reactions[5]. Therefore, effective technical strategies are needed to improve solar energy utilization efficiency and extend the lifetime of electron-hole pairs. Addressing these challenges represents a key research direction that requires breakthroughs in the field of photocatalysis[6]. To overcome these limitations, the construction of semiconductor heterojunctions has emerged as a potent strategy for modulating and optimizing photocatalytic performance. Through bandgap matching and interface interactions between different semiconductors, it can significantly broaden the light absorption range, promote carrier spatial separation, and photocatalytic activity can be further improved[7-8].

Bi_2MoO_6, a novel photocatalytic material[9-10], has been widely studied owing to its remarkable photocatalytic performance and efficient electron transfer capabilities[11-13]. The BMO mainly exists in α, β, and γ three crystal phases, and satisfies the chemical formula Bi_2O_3•nMoO_3. When n value takes 3, 2, 1, respectively, the corresponding chemical formulas are α-$Bi_2Mo_3O_{12}$, β-$Bi_2Mo_2O_9$, and γ-Bi_2MoO_6. α-$Bi_2Mo_3O_{12}$ is composed of a defective scheelite structure, where every three bismuth atoms have one vacancy, and molybdenum atoms exhibit tetrahedral local coordination. Similarly, β-$Bi_2Mo_2O_9$ is constructed based on a defective fluorite phase containing metal site vacancies; its molybdenum atoms also show tetrahedral local coordination features. While γ-Bi_2MoO_6 is a typical ternary aurivillius

ISSN 2616-5880 Vol. 7, Issue 1: 26-33, DOI: 10.25236/AJMC.2026.070105

compound, its crystal structure consists of alternating fluorite-type $(Bi_2O_2)^{2+}$ layers and $(MoO_4)^{2-}$ perovskite layers alternately arranged, forming a unique layered structure. This layered structure gives γ-BMO a stronger ability to capture visible light than the defective structures of α-BMO and β-BiMO [14].

Meanwhile, g-C_3N_4 is a highly promising photocatalyst[15-18] that is widely studied in photocatalysis and pollutant degradation[19], hydrogen production via water splitting [20-21], and CO_2 reduction [22-23]. However, there are also disadvantages, such as low visible light absorption efficiency and rapid recombination of photogenerated electron-hole pairs, which limit its further application. To enhance photocatalytic efficiency and facilitate the effective separation of photogenerated charges, the construction of a heterojunction is recognized as an effective approach to address the limitations of single-phase photocatalysts. The heterostructures, such as ZnO/g-C_3N_4 [24], g-C_3N_4/CdS [25], and TiO_2/g-C_3N_4 [26] have been widely applied. Recently, g-C_3N_4/BMO materials have also gained widespread interest. Li et al. successfully prepared g-C_3N_4/BMO heterostructures via a solvothermal approach and studied photocatalytic degradation in Rhodamine B (RhB) [27]. The experimental research shows that the heterostructure performs significantly better in the degradation of RhB under visible light in contrast to individual components, and the performance improvement is mainly due to the efficient separation of photogenerated carriers. However, current research on the effect of g-C_3N_4/BMO heterojunction interface chemical bonds on photocatalytic performance mainly relies on experimental characterization. Due to the limitations in the detection precision of experimental techniques, it is difficult to analyze the microscopic configuration of interfacial bonding, the migration path of photogenerated charges, and the energy variation patterns at the interface, thus limiting the understanding of the microscopic mechanism of the heterojunction.

In this work, first-principles calculations based on DFT are adopted to reveal the physical parameters of the g-C_3N_4/BMO heterojunction. The interfacial characteristics of g-C_3N_4/BMO are studied, and the charge transfer direction and the mechanism for the charge transfer direction at the interface are revealed, providing a theoretical foundation for understanding the separation and migration of electron-hole pairs. The results not only clarify the mechanisms for the improved performance in photocatalytic pollutant degradation but also offer theoretical insights for the design of oxide-based photocatalytic heterojunctions.

2. Computational methods

All simulations were carried out using the Vienna Ab initio Simulation Package (VASP) based on DFT [28-29]. The ion-electron interactions were described using the pseudopotential wavefunction (PAW) method, and the exchange-correlation potential is described using the Perdew-Burke-Ernzerhof (PBE) functional within the generalized gradient approximation (GGA) [30]. For the bulk structure of BMO, the plane-wave cutoff energy is set to 500 eV, and the k-point grid was 5×3×3. The cutoff energy for g-C_3N_4 was set to 500 eV with a 5×5×1 k-point grid, whereas a 3×3×1 grid was used for the g-C_3N_4/BMO (010), the relaxation convergence precision is set to 10^{-5} eV. At the same time, to eliminate the influence of interlayer interaction, a vacuum space of 15 Å was added along the z-axis. The results of the electronic structure were obtained using the VASPKIT package [31].

3. Results and discussion

3.1. Geometry structure and stability

To construct a heterojunction with lattice matching for g-C_3N_4 and the BMO (010) surface, we expanded the monolayer g-C_3N_4 to a 2×2×1, and the lattice mismatch degree is 3.54%. On this basis, we performed geometry optimization of the g-C_3N_4/BMO (010) heterojunction and studied its geometric and electronic structure. The space group of BMO is *Pca2₁*, belonging to the orthorhombic structure. The relaxed lattice constants are a = 5.617 Å, b = 16.625 Å, and c = 5.626 Å, which are also consistent with experimental and theoretical results [32-33]. The space group of g-C_3N_4 is p-6m2, and the optimized lattice constant is a = b = 4.759 Å, which is also consistent with experimental and theoretical data [34-35]. Given that previous experiments demonstrated enhanced photocatalytic performance on the exposed BMO (010) surface [36-37], we chose the BMO (010) surface to construct the g-C_3N_4/BMO(010) heterojunction (Figure 1).

ISSN 2616-5880 Vol. 7, Issue 1: 26-33, DOI: 10.25236/AJMC.2026.070105

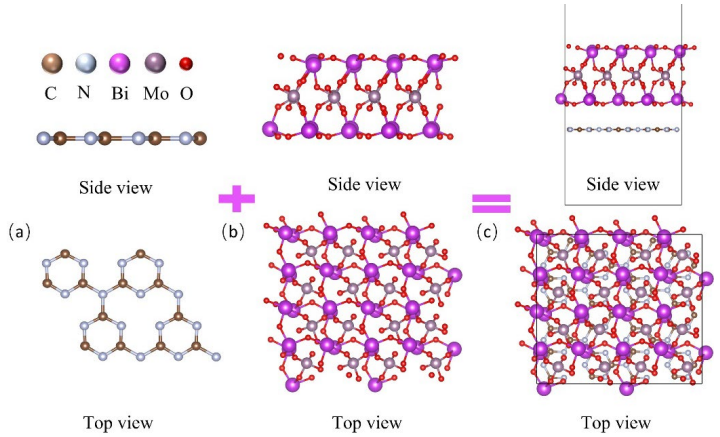

Figure 1: (a) 2×2×1g-C_3N_4, (b) BMO(010) surface, (c) g-C_3N_4/BMO(010) heterojunction.

3.2. Band structure

In order to study the interfacial interaction mechanism of the g-C_3N_4/Bi_2MoO_6(010) heterojunction, the band structures of bulk Bi_2MoO_6, the Bi_2MoO_6(010) surface, g-C_3N_4, and the g-C_3N_4/Bi_2MoO_6(010) heterojunction were calculated (Figure 2). The results show that all these systems are direct band gap semiconductors, with both the valence band maximum (VBM) and conduction band minimum (CBM) located at the Γ point of the Brillouin zone. Their band gap values are 1.95, 2.63, 1.56, and 0.97 eV, respectively. Although the calculated values are lower than the experimental ones due to the inherent underestimation of band gaps by the GGA-PBE functional, the trends in the VBM and CBM positions are consistent with previous reports [32,38-40]. Notably, the band gap of the g-C_3N_4/Bi_2MoO_6(010) heterojunction is significantly narrower than that of the individual g-C_3N_4 and Bi_2MoO_6 components, indicating a substantial enhancement in visible-light absorption. This band gap reduction facilitates electron transitions, increases the concentration of photogenerated electrons and holes, boosts photocatalytic activity, and induces a redshift of the absorption edge. Consequently, the redshift endows the g-C_3N_4/Bi_2MoO_6(010) heterojunction with superior optical properties.

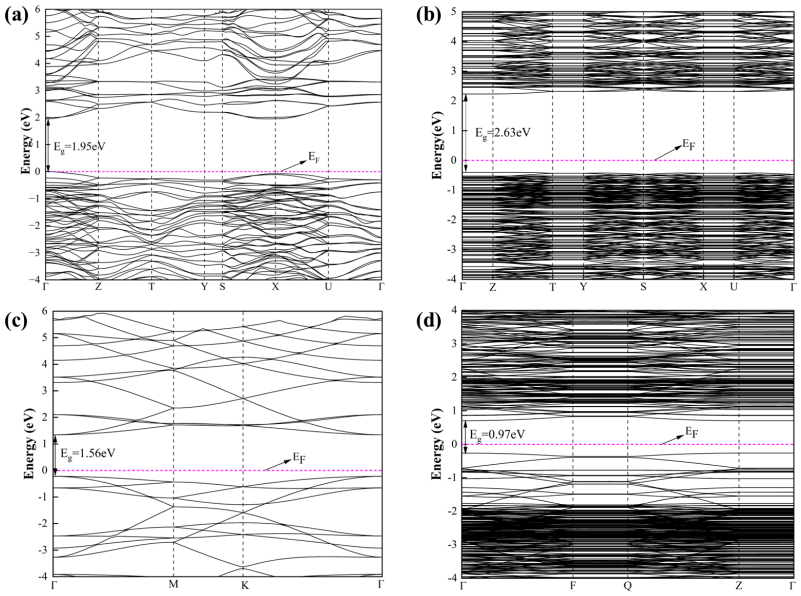

Figure 2: Band structure: (a) bulk BMO; (b) BMO(010) surface; (c) monolayer g-C_3N_4; (d) g-C_3N_4/BMO(010) heterojunction.

3.3. Density of States

To further analyze the properties of the g-C_3N_4/BMO heterojunction, we present in Figure 3 the calculated total density of states (TDOS) and partial density of states (PDOS). The DOS of bulk BMO and the BMO(010) surface shows significant contributions from O 2p orbitals in the valence band (VB),

ISSN 2616-5880 Vol. 7, Issue 1: 26-33, DOI: 10.25236/AJMC.2026.070105

which dominate the region near the Fermi level (E_F). This indicates that the VBM of BMO is mainly derived from O 2p orbitals, while the conduction band (CB) mainly originates from Mo 4d and Bi 6p orbitals (Figures 3a and 3b). Overall, p orbitals play a major role in both the VB and CB, serving as the primary contributors to electron transitions. The VBM of g-C_3N_4 is mainly derived from N 2p orbitals, while its CBM primarily arises from hybridization between C 2p and N 2p orbitals (Figure 3c). For the g-C_3N_4/BMO(010) heterojunction, the VBM is predominantly derived from the N 2p orbitals of g-C_3N_4, and the CBM mainly originates from the Bi 6p and Mo 4d orbitals of BMO (Figure 3d). Under visible-light irradiation, electrons in g-C_3N_4 are excited from the N 2p-dominated VBM to the CBM (which arises from C 2p orbitals). Driven by the built-in electric field at the interface, these electrons transfer from g-C_3N_4 to BMO, while holes simultaneously migrate from the O 2p-dominated valence band of BMO to the N 2p-dominated valence band of g-C_3N_4. This charge separation mechanism effectively suppresses carrier recombination and broadens the optical absorption in the visible region for the g-C_3N_4/BMO(010) heterojunction, thereby significantly improving its photocatalytic performance. Moreover, our analysis further reveals the interfacial charge transfer mechanism, which underpins the superior photoreactivity of the g-C_3N_4/BMO(010) heterojunction under visible light.

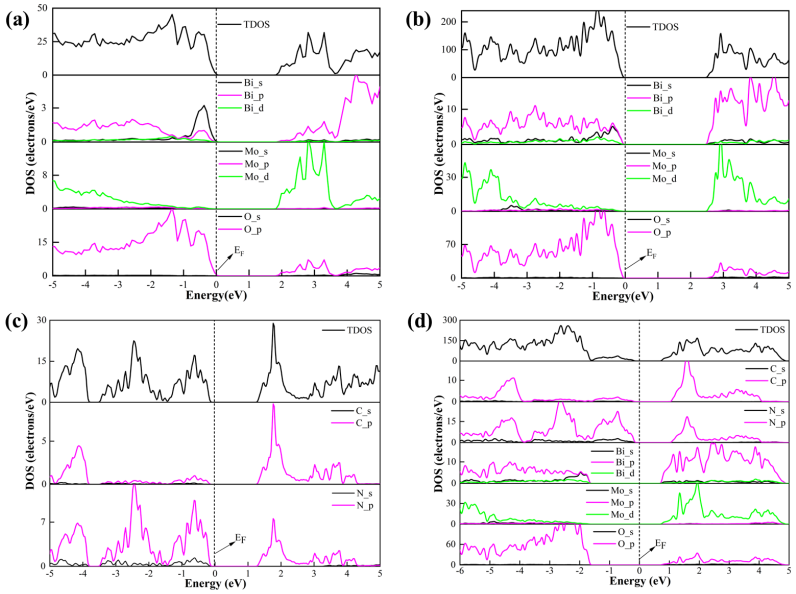

Figure 3: TDOS and PDOS: (a) Bulk BMO; (b) BMO (010) surface; (c) Monolayer g-C_3N_4; (d) g-C_3N_4/BMO(010) heterojunction.

3.4. Differential Charge Density and Work Function

To study the properties of charge transfer for the g-C_3N_4/BMO (010) heterojunction, Figure 4 illustrates the interfacial charge redistribution within the heterostructure, where the yellow and cyan surfaces correspond to electron density enrichment and deficiency. As shown in Figure 4, electrons mainly migrate between N-C sites of g-C_3N_4 and Mo and O atoms of BMO. The local charge change of Bi atoms is small due to the bonding characteristics constraining the charge redistribution. The charge density rearrangement occurs at the g-C_3N_4/BMO interface and forms distinct regions of electron accumulation and depletion. Moreover, the g-C_3N_4 surface shows charge depletion and forms hole-enriched active sites, while the Bi_2MoO_6 (010) surface has strong charge accumulation, forming electron-enriched active sites. The characteristics of charge spatial separation make electrons able to effectively migrate from the g-C_3N_4 layer to the BMO surface, which provides an efficient charge transfer pathway and facilitates the dissociation of photogenerated electron-hole pairs.

ISSN 2616-5880 Vol. 7, Issue 1: 26-33, DOI: 10.25236/AJMC.2026.070105

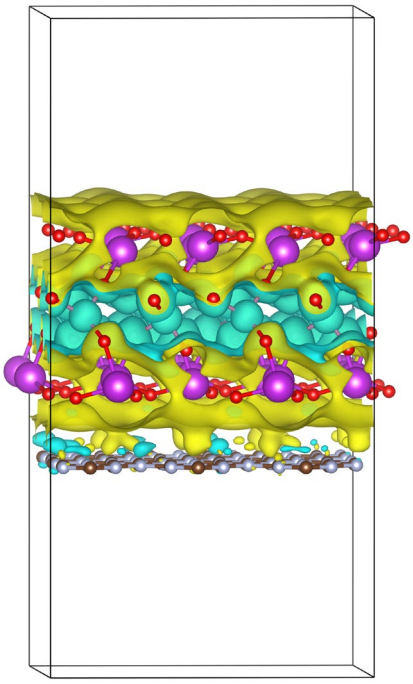

Figure 4: Differential charge density of g-C_3N_4/Bi_2MoO_6(010).

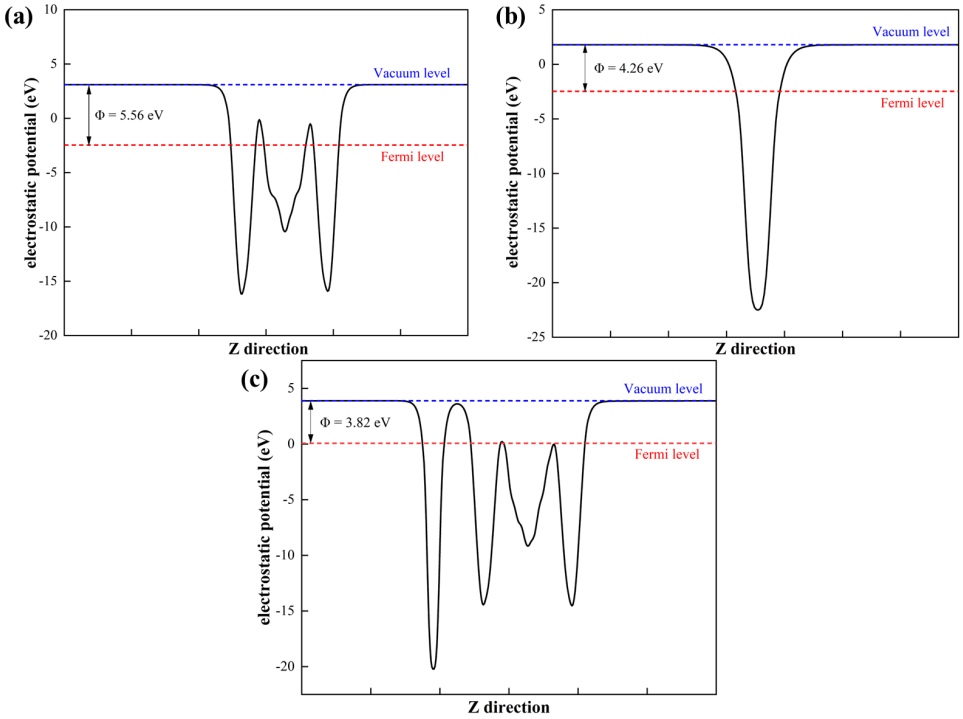

Figure 5: Work function: (a) BMO(010) surface; (b) monolayer g-C_3N_4; (c) g-C_3N_4/BMO(010) heterojunction.

The work function is a crucial parameter for evaluating electron emission capability. In heterojunction systems, it plays a key role in revealing interface charge transfer, the space charge field, and band bending. To clarify the band alignment and the separation efficiency of photogenerated electron–hole pairs in the heterojunction, the work functions of the BMO(010) surface, g-C_3N_4, and the g-C_3N_4/BMO(010) heterojunction were calculated, as shown in Figure 5. The calculated work functions are 5.56, 4.26, and 3.82 eV, respectively, which are consistent with existing research [32,41-42]. Owing to the relative positions of the Fermi levels, electrons migrate from g-C_3N_4 (higher Fermi level) to the BMO(010) surface (lower Fermi level) until Fermi level equilibration is reached. The electron-depleted g-C_3N_4 becomes positively charged, whereas the electron-enriched BMO(010) surface gains a negative charge; the resulting potential

ISSN 2616-5880 Vol. 7, Issue 1: 26-33, DOI: 10.25236/AJMC.2026.070105

gradient creates an interfacial electric field directed from g-C_3N_4 to BMO(010). These findings are consistent with the charge density difference analysis. The work function indicates spontaneous electron injection from g-C_3N_4 to the BMO(010) layer, creating an interfacial potential gradient that promotes charge separation, with electrons accumulating in BMO(010) and holes in g-C_3N_4. This significantly inhibits carrier recombination. These results provide a key theoretical basis for improving the photocatalytic performance of heterojunction materials.

4. Conclusion

In summary, first-principles methods based on DFT were used to study the photocatalytic mechanism of the g-C_3N_4/BMO(010) heterojunction. The results indicate that the heterojunction exhibits a direct band gap, which is significantly reduced compared to that of the individual components. These findings improve electron transition efficiency, and the reduced band gap induces a red shift of the absorption edge, which extends the visible-light response range. The synergistic effect overcomes the limitations of single-component semiconductors in visible-light absorption and ensures efficient solar energy capture and photocatalytic reactions. Moreover, the VBM of the heterojunction derives primarily from N 2p orbitals, whereas the CBM arises from the Bi 6p and Mo 4d orbitals of BMO(010). The charge density difference and work function demonstrate that the interfacial electric field effectively promotes the separation of electron–hole pairs and inhibits their recombination. This study provides a theoretical basis for the efficient photocatalytic properties of g-C_3N_4/BMO heterojunctions and offers clear guidance for the design of heterojunction-based photocatalytic materials.

References

[1] Zhang, T., Hu, C., Wu, J., Shen, B., Peng, S., Qi, Y. and Wang, Y. (2023) Fabrication, Structure, and Application of Sulfur-and Sulfide-Modified Bismuth Based Photocatalysts: A Review. Separation and Purification Technology, 323, 124352.

[2] Paracchino, A., Laporte, V., Sivula, K., Grätzel, M. and Thimsen, E. (2011) Highly Active Oxide Photocathode for Photoelectrochemical Water Reduction. Nature Materials, 10(6), 456-461.

[3] McFarland, E.W. and Metiu, H. (2013) Catalysis by Doped Oxides. Chemical Reviews, 113(6), 4391-4427.

[4] Zhang, M., Zhang, Y., Tang, L., Zhu, Y., Wang, J., Feng, C. and Zhang, Y. (2021) Synergetic Utilization of 3D Materials Merits and Unidirectional Electrons Transfer of Schottky Junction for Optimizing Optical Absorption and Charge Kinetics. Applied Catalysis B: Environmental, 295, 120278.

[5] Chen, L., Li, C., Zhao, Y., Wu, J., Li, X., Qiao, Z. and Wei, G. (2021) Constructing 3D Bi/Bi4O5I2 microspheres with rich oxygen vacancies by one-pot solvothermal method for enhancing photocatalytic activity on mercury removal. Chemical Engineering Journal, 425, 131599.

[6] Devi, L. G., Krishnamurthy, G. (2009) TiO_2/$BaTiO_3$-assisted photocatalytic mineralization of diclofop-methyl on UV-light irradiation in the presence of oxidizing agents. Journal of Hazardous Materials, 162(2-3), 899-905.

[7] Chen, F., Yang, Q., Zhong, Y., An, H., Zhao, J., Xie, T. and Zeng, G. (2016) Photo-reduction of bromate in drinking water by metallic Ag and reduced graphene oxide (RGO) jointly modified BiVO4 under visible light irradiation. Water Research, 101, 555-563.

[8] Peng, F., Zhou, Q., Zhang, D., Lu, C., Ni, Y., Kou, J. and Xu, Z. (2015) Bio-inspired design: Inner-motile multifunctional ZnO/CdS heterostructures magnetically actuated artificial cilia film for photocatalytic hydrogen evolution. Applied Catalysis B: Environmental, 165, 419-427.

[9] Yang, J., Xie, T., Mei, Y., Chen, J., Sun, H., Feng, S. and Chen, H. (2023) High-efficiency V-Mediated Bi_2MoO_6 photocatalyst for PMS activation: Modulation of energy band structure and enhancement of surface reaction. Applied Catalysis B: Environmental, 339, 123149.

[10] Xie, R., Fan, J., Fang, K., Chen, W., Song, Y., Pan, Y. and Liu, J. (2022) Hierarchical Bi_2MoO_6 microsphere photocatalysts modified with polypyrrole conjugated polymer for efficient decontamination of organic pollutants. Chemosphere, 286, 131541.

[11] Ma, Y., Jia, Y., Jiao, Z., Yang, M., Qi, Y. and Bi, Y. (2015) Hierarchical Bi_2MoO_6 nanosheet-built frameworks with excellent photocatalytic properties. Chemical Communications, 51(30), 6655-6658.

[12] Shen, X., Song, B., Shen, X., Shen, C., Shan, S., Xue, Q. and Li, S. (2022) Rationally designed S-scheme heterojunction of C_3N_4/Bi_2MoO_6/carbon fiber cloth as a recyclable, macroscopic and efficient photocatalyst for wastewater treatment. Chemical Engineering Journal, 445, 136703.

[13] Raja, A., Son, N. and Kang, M. (2021) Construction of visible-light driven Bi_2MoO_6-rGO-TiO_2 photocatalyst for effective ofloxacin degradation. Environmental Research, 199, 111261.

ISSN 2616-5880 Vol. 7, Issue 1: 26-33, DOI: 10.25236/AJMC.2026.070105

[14] Zhao, X., Xu, T., Yao, W. and Zhu, Y. (2009) Synthesis and photoelectrochemical properties of thin bismuth molybdates film with various crystal phases. Thin Solid Films, 517(20), 5813-5818.
[15] Fu, J., Chang, B., Tian, Y., Xi, F. and Dong, X. (2013) Novel C_3N_4–CdS composite photocatalysts with organic–inorganic heterojunctions: in situ synthesis, exceptional activity, high stability and photocatalytic mechanism. Journal of Materials Chemistry A, 1(9), 3083-3090.
[16] Liu, X., Ma, R., Zhuang, L., Hu, B., Chen, J., Liu, X. and Wang, X. (2021) Recent developments of doped g-C_3N_4 photocatalysts for the degradation of organic pollutants. Critical Reviews in Environmental Science and Technology, 51(8), 751-790.
[17] Wang, P., Xu, Z., Kong, Y., Tian, J. and Liu, C. (2025) Amino functionalized C doped g-C_3N_4 for boosting the adsorption and photoreduction of uranium (VI). Desalination, 119754.
[18] Fu, J., Yu, J., Jiang, C. and Cheng, B. (2018) g-C_3N_4-Based heterostructured photocatalysts. Advanced Energy Materials, 8(3), 1701503.
[19] Yan, S. C., Li, Z. S. and Zou, Z. G. (2009) Photodegradation performance of g-C_3N_4 fabricated by directly heating melamine. Langmuir, 25(17), 10397-10401.
[20] Yang, S., Gong, Y., Zhang, J., Zhan, L., Ma, L., Fang, Z. and Ajayan, P. M. (2013) Exfoliated graphitic carbon nitride nanosheets as efficient catalysts for hydrogen evolution under visible light. Advanced materials, 25(17), 2452-2456.
[21] Xu, J., Zhang, L., Shi, R. and Zhu, Y. (2013) Chemical exfoliation of graphitic carbon nitride for efficient heterogeneous photocatalysis. Journal of Materials Chemistry A, 1(46), 14766-14772.
[22] Dong, G. and Zhang, L. (2012) Porous structure dependent photoreactivity of graphitic carbon nitride under visible light. Journal of Materials Chemistry, 22(3), 1160-1166.
[23] Mao, J., Peng, T., Zhang, X., Li, K., Ye, L. and Zan, L. (2013) Effect of graphitic carbon nitride microstructures on the activity and selectivity of photocatalytic CO_2 reduction under visible light. Catalysis Science & Technology, 3(5), 1253-1260.
[24] Sun, J. X., Yuan, Y. P., Qiu, L. G., Jiang, X., Xie, A. J., Shen, Y. H. and Zhu, J. F. (2012) Fabrication of composite photocatalyst g-C_3N_4–ZnO and enhancement of photocatalytic activity under visible light. Dalton Transactions, 41(22), 6756-6763.
[25] Liu, J. (2015) Origin of high photocatalytic efficiency in monolayer g-C_3N_4/CdS heterostructure: a hybrid DFT study. The Journal of Physical Chemistry C, 119(51), 28417-28423.
[26] Zhou, X., Peng, F., Wang, H., Yu, H. and Fang, Y. (2011) Carbon nitride polymer sensitized TiO_2 nanotube arrays with enhanced visible light photoelectrochemical and photocatalytic performance. Chemical Communications, 47(37), 10323-10325.
[27] Lan, Y., Kong, Q., Wang, D., Ren, D., Fang, Z., Zhang, W. and Xiao, L. (2023). Construction of highly efficient 0D/2D Bi_2MoO_6/g-C_3N_4 heterojunctions for visible-light-driven photodegradation of 1-naphthol. Ceramics International, 49(2), 2149-2156.
[28] Kresse, G., Furthmüller, J. (1996) Efficient iterative schemes for ab initio total-energy calculations using a plane-wave basis set. Physical review B, Condensed matter, 54, 11169.
[29] Kresse, G. and Furthmüller, J. (1996) Efficiency of ab-initio total energy calculations for metals and semiconductors using a plane-wave basis set. Computational materials science, 6(1), 15-50.
[30] Perdew, J. P., Burke, K., and Ernzerhof, M. (1996) Generalized gradient approximation made simple. Physical Review Letters, 77(18), 3865.
[31] Wang, V., Xu, N., Liu, J. C., Tang, G. and Geng, W. T. (2021) VASPKIT: A user-friendly interface facilitating high-throughput computing and analysis using VASP code. Computer Physics Communications, 267, 108033.
[32] Opoku, F., Govender, K. K., van Sittert, C. G. C. E., Govender, P. P. (2018) Insights into the photocatalytic mechanism of mediator-free direct Z-scheme g-C_3N_4/Bi_2MoO_6 (0 1 0) and g-C_3N_4/Bi_2WO_6 (0 1 0) heterostructures: a hybrid density functional theory study. Applied Surface Science, 427, 487-498.
[33] Jing, T., Dai, Y., Wei, W., Ma, X. and Huang, B. (2014) Near-infrared photocatalytic activity induced by intrinsic defects in Bi_2MO_6 (M=W, Mo). Physical Chemistry Chemical Physics, 16(34), 18596-18604.
[34] Deng, M., Cao, X., Li, Z. and Tang, B. (2022) Hybrid triazine-based g-C_3N_4 (0 0 1)/anatase TiO_2 (0 0 1) heterojunction: Insights into enhanced photocatalytic mechanisms via DFT calculation. Journal of Photochemistry and Photobiology A: Chemistry, 423, 113577.
[35] Ashwini, M. A., Sagadevan, S., Fatimah, I., Paiman, S., Upadhyay, S., Garg, S. and Johan, M. R. (2025) Photocatalytic performance of TiO_2/g-C_3N_4 nanocomposite modified with carbon quantum dots for effective dye degradation: Experiments and DFT studies. Journal of Alloys and Compounds, 1025, 180296.
[36] Zheng, Y., Duan, F., Wu, J., Liu, L., Chen, M. and Xie, Y. (2009) Enhanced photocatalytic activity of bismuth molybdates with the preferentially exposed (0 1 0) surface under visible light irradiation.

ISSN 2616-5880 Vol. 7, Issue 1: 26-33, DOI: 10.25236/AJMC.2026.070105

Journal of Molecular Catalysis A: Chemical, 303(1-2), 9-14.
[37] Long, J., Wang, S., Chang, H., Zhao, B., Liu, B., Zhou, Y. and Huang, W. (2014) Bi_2MoO_6 nanobelts for crystal facet-enhanced photocatalysis. Small, 10(14), 2791-2795.
[38] Kistan, A., Narmatha, S., Chitra, M. and Mayavan, L. (2025) A novel mesoporous Bi_2MoO_6/g-C_3N_4 nanocomposite as an effective photocatalyst against toxic organic pollutants. Diamond and Related Materials, 151, 111841.
[39] Cao, C., Huang, Y., Tian, L., Wang, J., Yang, M., Meng, Q. and Zhang, Y. (2025) 2D/2D Bi_2MoO_6/g-C_3N_4 direct Z-scheme Van der Waals heterojunction photocatalyst for boosting nitrogen fixation. Journal of Environmental Chemical Engineering, 13(1), 115019.
[40] Xu, L., Huang, W. Q., Wang, L. L., Tian, Z. A., Hu, W., Ma, Y. and Huang, G. F. (2015) Insights into enhanced visible-light photocatalytic hydrogen evolution of g-C_3N_4 and highly reduced graphene oxide composite: the role of oxygen. Chemistry of Materials, 27(5), 1612-1621.
[41] Zhou, G., Tian, Z., Sun, H., Zhang, J., Zhao, H., Li, P. and Sun, H. (2020) Understanding the photocatalytic mechanisms of the BiOI/Bi_2MoO_6 and BiOCl/Bi_2MoO_6 heterostructures: first-principles study. Journal of Physics and Chemistry of Solids, 146, 109577.
[42] Zhu, B., Cheng, B., Zhang, L. and Yu, J. (2019) Review on DFT calculation of s-triazine-based carbon nitride. Carbon Energy, 1(1), 32-56.